

***Final Draft***  
**of the original manuscript:**

Bachmann, M.; Carstensen, J.; Bergmann, L.; dos Santos, J.F.; Wu, C.S.;  
Rethmeier, M.:

**Numerical simulation of thermally induced residual stresses in  
friction stir welding of aluminum alloy 2024-T3 at different  
welding speeds**

In: The International Journal of Advanced Manufacturing Technology  
(2016) Springer

DOI: 10.1007/s00170-016-9793-8

# Numerical simulation of thermally induced residual stresses in friction stir welding of aluminum alloy 2024-T3 at different welding speeds

Marcel Bachmann · Jan Carstensen ·  
Luciano Bergmann · Jorge F. dos Santos ·  
Chuan Song Wu · Michael Rethmeier

Received: date / Accepted: date

**Abstract** The paper deals with a numerical finite element simulation of the residual stress evolution in friction stir welding of 6mm thick aluminum alloy AA2024-T3. The transient thermal field during the welding process was calculated with the commercial code COMSOL Multiphysics 5.0. Therefore, a thermal-pseudo-mechanical (TPM) heat source was implemented. A subsequent mechanical simulation was performed with varying hardening models for different welding speeds of 60 mm/min and 300 mm/min. The influence of softening effects of the material, which were due to hardening precipitation dissolution associated to the heating were also investigated. Experiments in terms of thermocouple measurements as well as Vickers hardness and X-ray measurements of the residual stresses were conducted and compared to the numerical results. A qualitatively as well as quantitatively good agreement was found for different applied welding speeds.

**Keywords** friction stir welding · residual stress · finite element simulation

**PACS** 81.20.Vj (joining, welding) · 02.70.Dh (FEM)

## 1 Introduction

Friction stir welding (FSW) is a modern solid-state welding process invented in 1991 at The Welding Institute (TWI) [1] as an alternative to conventional joining technologies especially for materials being known to be hardly weldable. Nowadays, it is frequently used in the shipbuilding, aerospace, automotive and railway industries [2].

---

M. Bachmann, M. Rethmeier  
BAM Federal Institute for Materials Research and Testing, Unter den Eichen 87, 12205 Berlin, Germany  
E-mail: marcel.bachmann@bam.de

L. Bergmann, J. Carstensen, J.F. dos Santos  
Helmholtz-Zentrum Geesthacht, Institute of Materials Research, Materials Mechanics,  
Solid-State Joining Processes, Max-Planck-Str. 1, 21502 Geesthacht, Germany

C.S. Wu  
Institute of Materials Joining, Shandong University, Jinan 250061, China

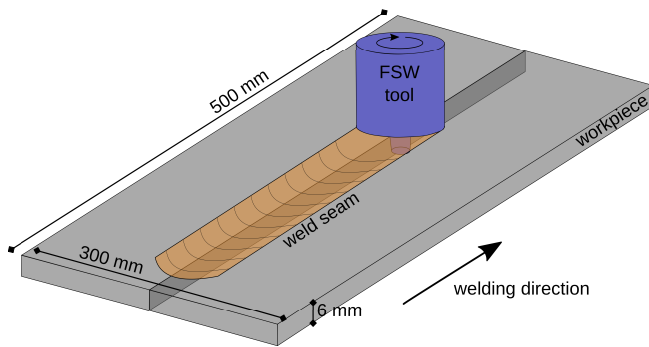


**Fig. 1** Schematic friction stir welding process.

In the FSW process, a rotating non-consumable tool penetrates the material and creates the joint. Heat is generated at the contact surface between the tool and the workpiece by friction as well as by volumetric plastic deformation. Furthermore, the pin stirs the material and supports the transport of plasticized material from its front side to the trailing side [3, 4], see Fig. 1.

As the physical phenomena occurring in FSW are strongly coupled, e.g. the heat generation depends on the material flow and the conditions in the contact region between tool and workpiece and vice-versa [5], numerical simulations are a promising tool to gain insights into the process being inaccessible experimentally. All kinds of numerical simulations in welding, let it be purely thermal, mechanical, microstructural or fluid, require an accurate prediction of the thermal field during all stages of the welding process. In the last years, a lot of different thermal models to account for the special heat generation mechanisms in FSW were developed.

An analytical expression model for the heat generation in FSW with conical tool shoulder and cylindrical pin is proposed in [6]. In [7, 8], experimentally measured values of the input torque were used for the description of the heat source. Analytical expressions to account for the velocity in FSW were used in [9]. A frequently used method to include Coulomb friction depending on the mechanical pressure in the contact zone between workpiece and FSW tool is described in [10].

In CFD simulations, the material flow around the rotating tool pin depending on the viscous state of the material in two or three dimensions can be predicted depending on the tool geometry, e.g. in [11, 12], for aluminum alloys [13–15] or mild steel [16]. A coupled model consisting of material flow and temperature simulations of the FSW process designed for experimental optimization purposes was shown in [17]. An investigation focusing on the contact conditions between pin and workpiece was conducted in [18].

One of the first attempts to establish Arbitrary-Lagrangian-Eulerian (ALE) formulations in FSW modeling was done in [19]. A material flow visualization method in FSW using the particle tracing algorithm is presented in [20]. Here, different kinematic frameworks (Eulerian, Lagrangian, ALE) were assumed for the different weld regions (workpiece, heat affected zone, stir zone, pin). A similar approach to simulate non-circular pin geometries was published in [21]. Moreover, the work [22] gives a detailed description of a generalized ALE approach in FSW. A comparison between a solid and a fluid approach in FSW simulation for a triangu-

lar pin profile is presented in [23] showing similar results. The ALE methodology was also used in the finite element software package Forge3D to simulate main thermo-mechanical phenomena occurring during FSW including contact effects between pin and workpiece [24].

A different way of determining the heat input in FSW numerically was proposed by [5]. The Thermo-Pseudo-Mechanical (TPM) heat source, which was also used in this investigation, combines aspects of purely thermal and mechanical analysis to predict the energy input into the workpiece with the material yield stress as the only unknown parameter being able to be used for multiple process parameters without the need for repetitive calibrations. A very good overview on thermal models and beyond in FSW can also be found in recent review articles [25–27]. A comparison between different types of heat source geometries and topologies for the bobbin tool was examined in [28]. The influence of the tool diameter on the temperature was investigated in [29].

In many investigations regarding residual stress development, it is common praxis to decouple the thermal and the thermo-mechanical problem in welding leading to a one-way coupling between both calculation steps and also to neglect the material flow. [30] gives a wide overview on different approaches in numerical residual stress calculation with varying hardening laws and softening models for precipitate hardened aluminum alloys. Another very nice recent overview on challenges in thermo-mechanical related analysis of friction stir welding can be found in [31].

The present paper deals with the thermally induced residual stress development in friction stir weld of aluminum alloy 2024-T3 under different welding velocities. The thermal degradation of the specimen was considered and the impact on the choice of relevant numerical models of the plastic behavior was also investigated and compared to results of welding experiments.

## 2 Experimental conditions

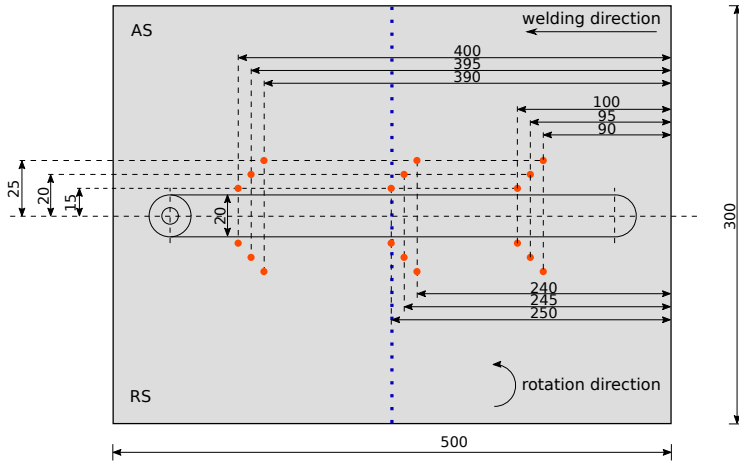
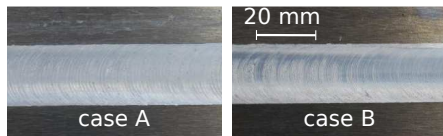
The friction stir welds were performed with an aluminum alloy AA2024-T3. The geometric dimensions were 500 mm in length, 2×150 mm in width, and 6 mm in depth. The processing velocities were 60 mm/min and 300 mm/min, respectively, with a constant tool rotation of 600 rotations per minute. The tool shoulder was 20 mm in diameter with a 1.2 mm deep spiral on its contact surface. The threaded triflat tool pin had a length of 5.8 mm and a diameter of 8 mm being conically reduced with an angle of 10°. An analysis of the effect of the tool pin profile as well as the axial force in FSW of aluminum alloy can be found in [32]. The experiments were conducted with a Robotic Gantry FSW System at Helmholtz-Zentrum Geesthacht. A summary of the processing parameters can be seen in Tab. 1.

The locations of the thermocouple and X-ray measurements of the thermal cycle and the residual stresses after cooling down and unclamping can be seen in Fig. 2. As the results of the temperature measurements at the positions in welding direction and also between the retreating and advancing side were differing only up to around 25 K, the redundant informations were skipped hereafter.

The top surface of the produced welds can be seen in Fig. 3. They were found to be free of surface defects, smooth and without a welding flash.

**Table 1** Process parameters used in this investigation.

	tool rotation RPM	welding speed mm/min	axial force kN	weld pitch 1/mm
case A	600	60	13	10
case B	600	300	18.5	2

**Fig. 2** Positions of the measurements of the temperature (points) and the residual stresses (dotted line).**Fig. 3** Top surface of the welds with welding parameters according to Tab. 1.

### 3 Numerical Modeling

The aim of this paper was to calculate the developing thermally induced residual stresses in friction stir welding of aluminum alloy 2024-T3 for different welding velocities. Therefore, the finite element simulation with the commercial software package COMSOL Multiphysics 5.0 consists of three subsequent simulation steps:

- First, the transient welding temperature field was calculated.
- Based on that, the thermally induced softening of the material was determined.
- Finally, the structural mechanics quantities were calculated after the whole process including dwelling stages, welding, cooling stage, and unclamping.

The complete welding procedure consisted of several steps: (a) a 10 s dwelling time before moving the rotating FSW tool, (b) the welding stage itself with constant processing velocity, (c) a 2 s dwelling time after the welding process, (d) cooling down, and (e) unclamping.

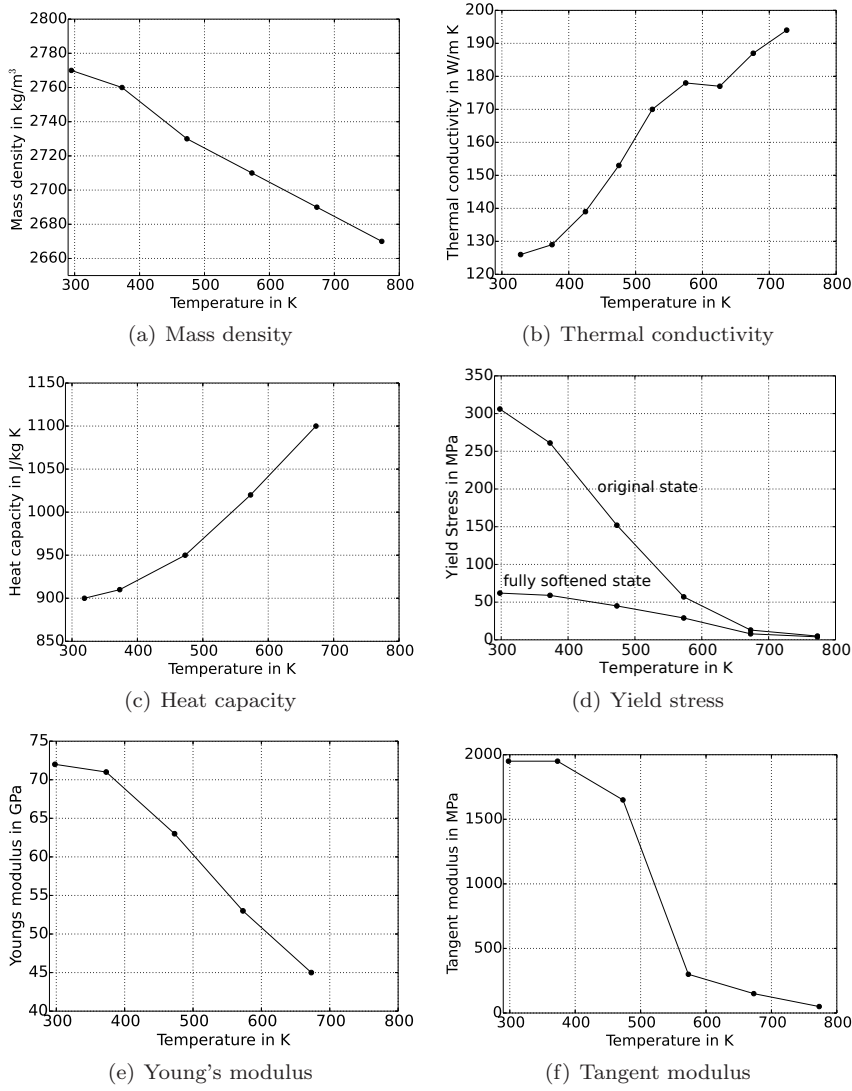


**Fig. 4** Material properties of aluminum alloy 2024 taken from [30], as collected from [34,35].

The simulation mesh for the two calculation cases consisted of 29,000 and 68,000 hexahedral elements for case A and B, respectively with quadratic shape functions. The temperature field was solved with the PARDISO direct solver which lead to 260,000 and 380,000 degrees of freedom for the two cases. The remaining quantities were solved together with the MUMPS direct solver with around  $1 \cdot 10^6$  and  $3.6 \cdot 10^6$  degrees of freedom, respectively.

The material properties depending on the temperature are summarized in Fig. 4. The coupling of thermal and thermo-mechanical parts of the simulation with respect to the thermally induced softening of the material was adopted from

the work presented in [30], which was later also used for crack propagation with the same material [36].

### 3.1 Heat equation

For the welding temperature field  $T$ , the transient heat equation was solved:

$$\rho c_p \frac{\partial T}{\partial t} + \rho c_p \mathbf{u} \cdot \nabla T = \nabla \cdot (\lambda \nabla T). \quad (1)$$

Herein,  $\rho$ ,  $c_p$ ,  $t$ ,  $\mathbf{u}$  and  $\lambda$  are the density, heat capacity, time, velocity and thermal conductivity, respectively.

The thermal load was realized by a thermal pseudo-mechanical surface heat source proposed by [5]. Here, the heat input depends solely on the yield stress  $\sigma^y$ , the tool rotation  $n$  and the radial distance  $r$  to the tool rotation axis:

$$\frac{\dot{q}}{A} = \omega r \tau(T) = \left( \frac{2\pi n}{60} \right) r \frac{\sigma^y}{\sqrt{3}}. \quad (2)$$

According to the work in [14], a contribution to the net heat input into the workpiece caused by plastic deformation due to the material flow as well as by the rotation of the tool pin was neglected.

The thermal boundary conditions at the surfaces of the specimen are summarized in Eq. (3).

$$-\mathbf{n} \cdot (-\lambda \nabla T) = \begin{cases} 0 & \text{symmetry surface} \\ h(T_0 - T) & \text{bottom surface} \\ h(T_0 - T) + \epsilon \sigma_B (T_0^4 - T^4) & \text{else} \end{cases} \quad (3)$$

with the heat transfer coefficient  $h$ , which is  $10 \text{ W/m}^2 \text{ K}$  at all surfaces being in contact with air except the bottom surface, where a 30 times higher value was applied to account for the influence of heat losses into the backing plate, which was adjusted to the conducted experimental temperature fields. The ambient temperature  $T_0$  was assumed to be  $300 \text{ K}$ . Furthermore, radiative heat transfer was assumed on all surfaces but the bottom side with a surface emissivity  $\epsilon$  of  $0.25$  and the Stefan-Boltzmann constant  $\sigma_B$ . As the process was modeled half-symmetric, the symmetry surface was considered as adiabatic. For the heat source, the upper stress curve from Fig. 4(d) was used.

### 3.2 Softening behavior due to thermal loads

As the material strength is heavily affected by the heat input due to the rotational speed of the FSW tool, the dissolution of the hardening precipitates was accounted for using a computational model presented by [37]:

$$\frac{\partial t_{eq}}{\partial t} = \frac{1}{t_{ref}} \exp \left\{ \frac{Q_{eff}}{T} \left[ \frac{1}{T_i} - \frac{1}{T_{ref}} \right] \right\}, \quad (4)$$

$$t_{eq} = \sum_{i=1}^N \frac{\Delta t_i}{t_i^*} = \sum_{i=1}^N \frac{\Delta t_i}{t_{ref} \exp \left\{ \frac{Q_{eff}}{T} \left[ \frac{1}{T_i} - \frac{1}{T_{ref}} \right] \right\}}. \quad (5)$$

This causes a significant softening of the material which is expressed by a decrease of the yield stress curves. The numerical method to account for this effect interpolates linearly between a maximum and minimum yield stress curve that describe the original and the fully softened state, respectively, see Fig. 4(d). The interpolation considers an equivalent time of heat treatment  $t_{eq}$  of the process and the determined amount of dissolution of hardening precipitates, consequently. The fraction of the dissolution of the hardening precipitates is called  $X_d$ ;  $t_{ref}$  is the time for a total dissolution at the reference temperature  $T_{ref}$ . The model relates the heating time of the material above a reference temperature to the time for a complete dissolution of precipitation hardening.  $Q_{eff}$  is the activation energy for the precipitation dissolution.

$$\frac{f}{f_0} = 1 - X_d = 1 - \sqrt{t_{eq}} \quad (6)$$

$$\sigma^y = \sigma_{min}^y + \frac{f}{f_0} (\sigma_{max}^y - \sigma_{min}^y) \quad (7)$$

The same approach can be used for the hardness of the material:

$$HV = HV_{min} + \frac{f}{f_0} (HV_{max} - HV_{min}). \quad (8)$$

The values for the parameters of the softening model are summarized in Tab. 2.

**Table 2** Modeling parameters for the softening due to thermal dissolution of precipitation hardening.

$T_{ref}$	623 K
$t_{ref}$	16 s
$Q_{eff}$	70.52 kJ/mol
$HV_{min}$	120 HV
$HV_{max}$	161 HV
$\sigma_{min/max}^y$	see Fig. 4(d)

### 3.3 Structural mechanics

The applied transient thermal fields from the previous calculation steps acted as a load for the subsequent structural mechanics simulation. The coefficient of thermal expansion was  $2.32 \times 10^{-5} \text{ K}^{-1}$  [8]. The present temperature as well as the material softening due to the dissolution of precipitates determine the mechanical behavior of the material, which was assumed to be representable by an elastoplastic

calculation with a standard  $J_2$  flow theory. The Young's modulus in Hooke's law was depending on temperature, see Fig. 4(e). The Poisson ratio was 0.33. Small plastic strains were assumed in the calculation and a standard von Mises yield criterion was adopted.

Three different scenarios were considered for both cases from Tab. 1: (a) linear isotropic hardening, (b) linear isotropic hardening without thermal softening, and (c) perfectly plastic behavior without hardening.

For the isotropic hardening model, the yield stress depends on the temperature, the softening state, and also linearly on the effective plastic strain with a temperature-depending isotropic tangent modulus, see Fig. 4(f). The initial yield stress was taken from the interpolation of the data shown in Fig. 4(d) respecting the approach described in section 3.2. In the case of perfectly plastic behavior, there was no hardening effect and the slope of the stress-strain curve beyond the elastic region was zero.

The workpiece was rigidly clamped at the outer lateral boundary during the welding process. At the bottom side, deformations in vertical direction were prevented. After welding and cooling down to room temperature, the welding fixture was released by replacing the clamping boundary condition with springs. In [38], the influence of different clamping scenarios on residual stresses and distortion was investigated.

## 4 Results & Discussion

### 4.1 Heat distribution

The values of the surface heat input due to the frictional heat of the traversing rotating FSW tool can be seen in Fig. 5. In both cases, the heat input for constant radial distance is higher at the front side of the tool, where the local temperature is certainly lower compared to the trailing side. The heat source depends on the yield stress which is amongst others a function of the local temperature field. This leads to increased yield stress values there. In the case of the lower welding speed, the temperatures of the material just entering the area of the tool shoulder at the

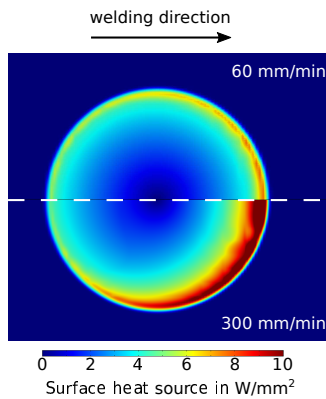
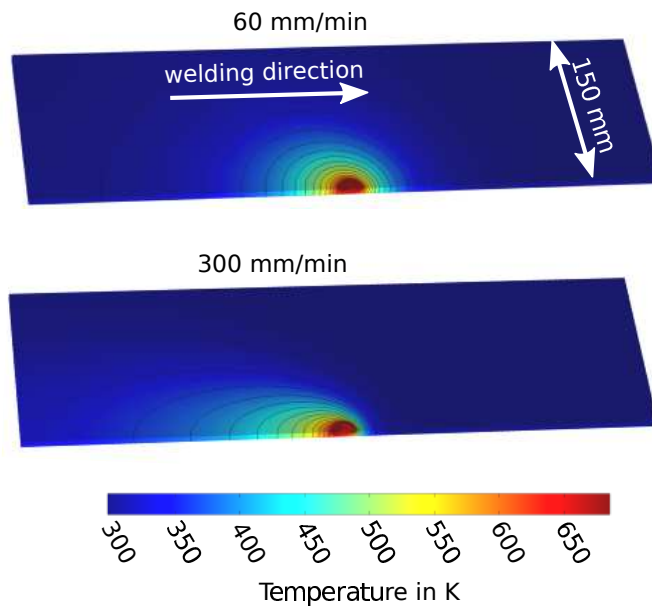


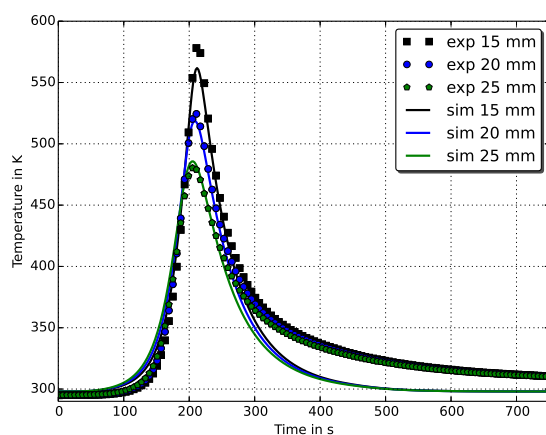
Fig. 5 Values of the surface heat source for two welding velocities.



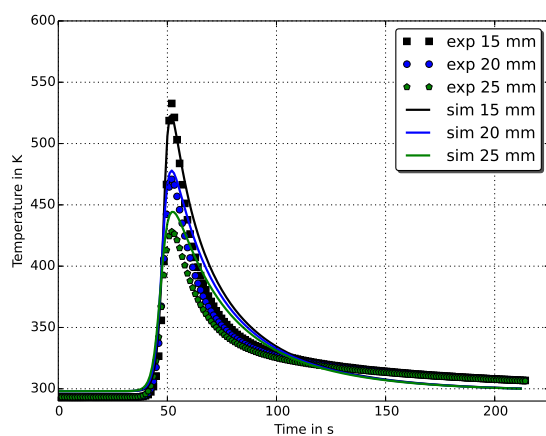
**Fig. 6** Temperature field during the process with the heat source at mid-plate position.

front side was higher compared to the higher welding speed. Thus the yield stress was reduced in this case leading to lower values of the heat source for a single moment in time, see also eq. (2) and Fig. 4(d). Nevertheless, the total integral heat input was much higher for the lower welding speed, approximately scaling with the quotient of the welding speeds. Instant temperature distributions for the moment when the tool was at the mid-plate position can be seen in Fig. 6. The isothermal lines are nearly circular for the low welding speed whereas they are more elliptical in the case of the higher speed with the same applied tool rotation.

A comparison of the experimentally observed with the numerically calculated transient temperature distributions for three positions at the top surface with a lateral distance of 15 mm, 20 mm, and 25 mm can be seen in Fig. 7. The more pronounced temperature decrease to the lateral sides for the higher welding speed already seen from Fig. 6 is also visible here. The numerical model can capture the thermal behavior very well. In case A, the maximum temperature agrees with the experimental measurements and there are only minor differences in the lower temperature region. In case B, the model predicts to a small amount lower maximum temperatures and captures the temperature decay with time realistic.



(a) Case A



(b) Case B

**Fig. 7** Comparison of the experimentally observed and numerically calculated transient temperature characteristics for both cases investigated at distances of 15 mm, 20 mm, and 25 mm from the weld centerline.

#### 4.2 Thermally induced material softening

The ratio of the thermally induced softening of the material due to a dissolution of precipitation hardening according to Eqs. (4) - (7) is shown in Fig. 8. A softening fraction of zero corresponds to the unaltered original state whereas a complete softening is associated to the lower yield stress curve in Fig. 4(d). For the lower welding speed, the material was heated sufficiently long to be completely softened in the region below the tool shoulder. For the higher welding speed, the material was softened up to around 80 % at the top surface, except the area of the first dwelling stage with a corresponding longer residence time of the tool.

The local distributions of the yield stress were found by an interpolation according to Eq. (7) and also by the dependence on temperature. For the two welding

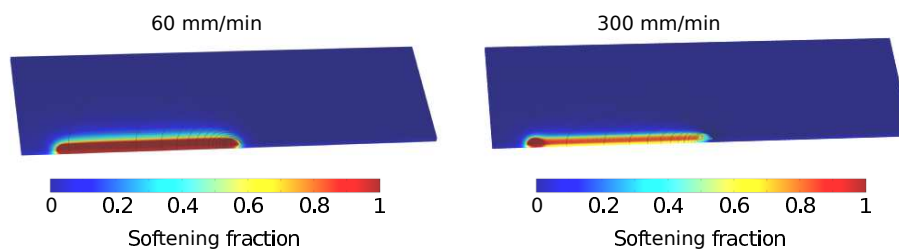


Fig. 8 Softening fraction during the process with the heat source at mid-plate position.

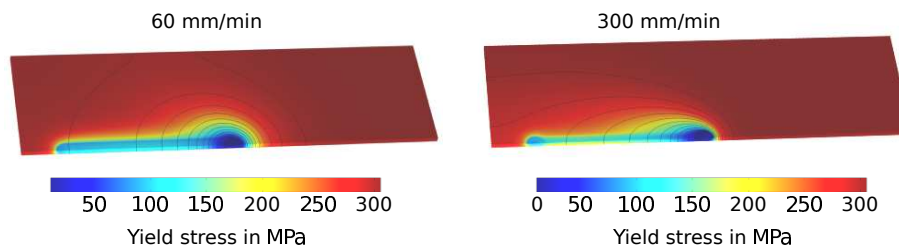


Fig. 9 Yield stress during the process with the heat source at mid-plate position.

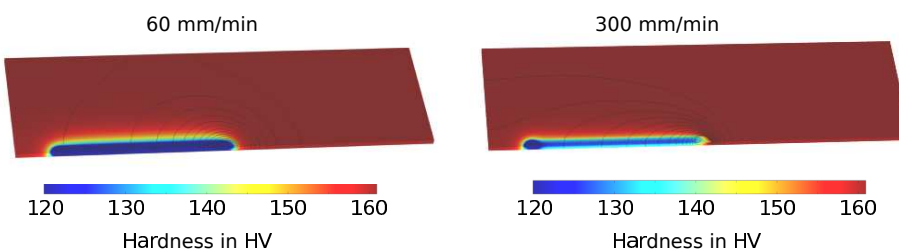
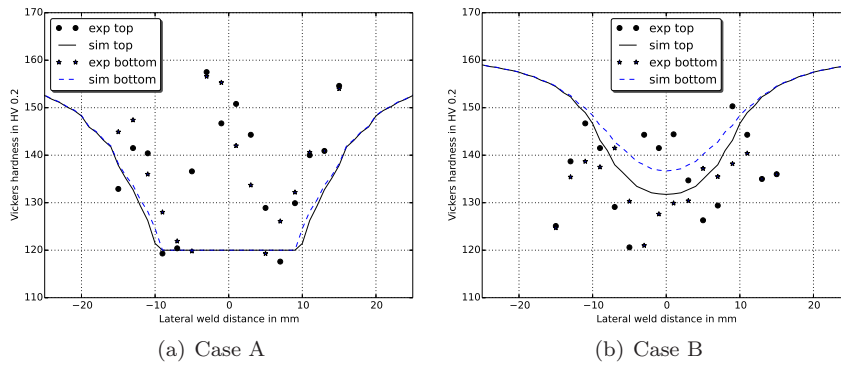


Fig. 10 Hardness values during the process with the heat source at mid-plate position.

speeds, the local variations of the yield stress during the welding tool passes the mid-plate position can be seen in Fig. 9. Due to the lower heat load in case B, the yield stress on the weld centerline behind the tool is higher compared to case A which is mainly associated to the different softening behavior. In the near vicinity of the tool, the influence of the higher temperatures is observable by a wider zone of temporary lowered yield stress associated to earlier plasticizing. This effect makes the whole process self-limiting in terms of the potential heat input.

Corresponding to the calculated softening of the material, the Vickers hardness can be calculated according to Eq. (8). Their distribution can be seen in Fig. 10 not regarding any aging effects during or after the cooling stage that can be seen in the experimental measurements, see Fig. 11. Of course, the results are in analogy to the results presented for the softening fraction in Fig. 8 with the lowest values in each case occurring on the weld centerline top surface where the heat load is maximum.



**Fig. 11** Vickers hardness perpendicular to the welding direction taken from macrographs and compared to numerical results from mid-plate position. Negative coordinate values correspond to the advancing sides whereas positive coordinate values correspond to the retreating sides. The top curves were taken from 1.5 mm below the top surface and the bottom curves were taken from 1.5 mm above the bottom surface.

#### 4.3 Mechanical stress distribution

During the welding procedure, the maximum stresses occur in front of the welding tool as can be seen in Fig. 12 which are compressive in nature as known from other welding processes. Material in the vicinity of the tool was heated up by the frictional work leading to plastification and yielding. The relatively colder areas prevent an expansion thus in consequence forming mechanical stresses. For the lower welding speed, the von Mises stresses to the lateral sides are higher and also

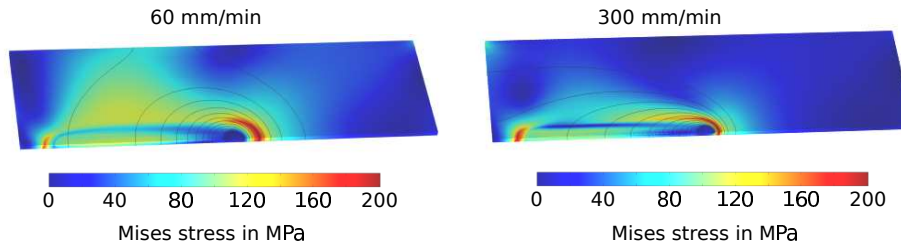


**Fig. 12** Mises stress during the process with the heat source at mid-plate position using an isotropic hardening rule.

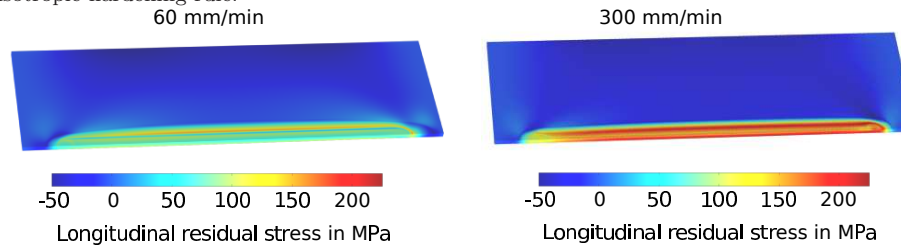


**Fig. 13** Longitudinal residual stresses after cooling down and unclamping an isotropic hardening rule.

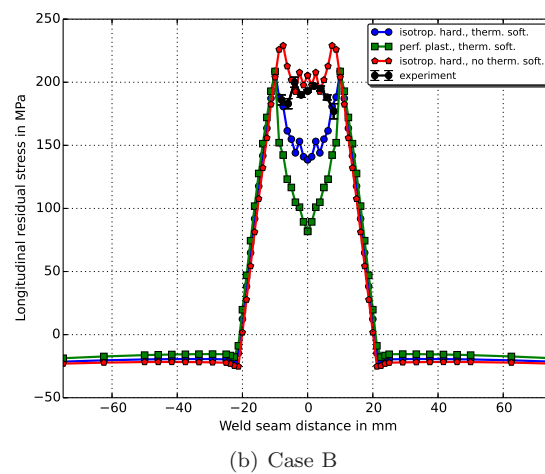
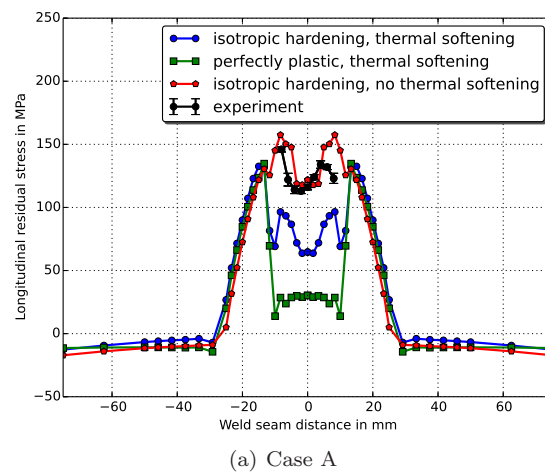


**Fig. 14** Comparison of the experimentally observed and numerically calculated longitudinal residual stresses for both cases investigated after cooling down and unclamping.

the highly stressed area in front of the tool is larger when compared to the faster welding speed, which can be explained by the higher energy input per unit length.

After cooling down and unclamping, the longitudinal residual stresses are on a higher level for the faster welding velocity, see Fig. 14, but remain concentrated within a smaller lateral distance. This is in accordance to the work in [39]. The reason for that is the shorter time for heat diffusion perpendicular to the welding direction in case of higher welding speeds which leads to higher spatial temperature gradients there during welding and higher mechanical stresses after cooling down. Aside from the different temperature distributions, the higher tensile stress values are also a consequence of the stronger shrinkage prevention of the surrounding material in the vicinity of the FSW tool compared to the lower welding speed with corresponding highly developed thermal softening, see Fig. 4(d).

The differences in the developing longitudinal residual stresses at the top surface at mid-plate position depending on the implemented hardening rule and the comparison to the experimentally obtained stress values in longitudinal direction can be seen in Fig. 14. X-ray measurements with sufficiently small error were restricted to the area under the FSW tool which might be due to the rolling process of the material. Transversal residual stresses were also recorded but disregarded here as their maximum was below  $\pm 50$  MPa in all cases.

For all three scenarios at constant velocity presented, the stress values outside the FSW tool are very similar. Larger differences occur within the region of the welding tool. The smallest residual stress values were obtained with an assumed negligence of hardening (constant value in the plastic region of the stress-strain curve) which is referred to as perfectly plastic. The highest stress values were obtained when thermal softening was neglected in combination with isotropic hardening and a bilinear representation of the stress-strain curve. The resulting stresses in the region under the FSW tool for the isotropic hardening model also respecting the thermal softening were in between the two other cases. Moreover, the experimental values were found to be comparable to the two latter cases.

Comparing cases A and B, the occurring stresses were found to be higher for the latter as it was also seen in Fig. 13. One can conclude that neglecting the hardening effect beyond yielding is oversimplifying the process whereas the isotropic hardening model can capture the qualitative and also the quantitative stress development quite satisfactory with absolute differences  $\pm 50$  MPa.

## 5 Summary

A sequentially coupled thermo-mechanical model of friction stir welding with emphasis on different hardening rules and thermal softening behavior was investigated for two different welding velocities. A comparably simple surface heat source approach was adopted and the results obtained were in good agreement with experimental measurements.

Based on the transient temperature distribution for the two cases investigated, thermal softening and the development of residual stresses after cooling down the workpiece and unclamping were calculated with different scenarios. An isotropic hardening model showed good agreement to X-ray measurements of the residual stresses which were higher for the faster welding speed. The region with a remarkable influence of the thermal load in terms of residual stresses was found to be restricted to the near vicinity of the FSW tool with a lateral distance of around twice its radius.

**Acknowledgements** The authors are grateful for the financial support for this research from the Sino-German Center for the Promotion of Science (Grant No. DFG 739) as well as the Deutsche Forschungsgemeinschaft (Grant No. RE 1648/5-1). We would also like to thank the Helmholtz-Zentrum Geesthacht for their support with the experimental work.

## References

1. W.M. Thomas, E.D. Nicholas, J.C. Needham, M.G. Murch, P. Temple-Smith, C.J. Dawes: Friction stir butt welding. International Patent Application no. PCT/GB92/02203, Decem-

- ber 1991
2. W.M. Thomas, E.D. Nicholas: Friction stir welding for the transportation industries, *Materials & Design* 18 (1997), pp. 269 – 273
  3. R.S. Mishra, Z.Y. Ma: Friction stir welding and processing, *Materials Science and Engineering: R* 50 (2005), pp. 1 – 78
  4. R. Nandan, T. Debroy, H. K. D. H. Bhadeshia: Recent advances in friction-stir welding-process, weldment structure and properties, *Progress in Materials Science* 53 (2008), pp. 980 – 1023
  5. H. Schmidt, J.H. Hattel: Thermal modelling of friction stir welding, *Scripta Materialia* 58 (2008), pp. 332 – 337
  6. H. Schmidt, J.H. Hattel, J. Wert: An analytical model for the heat generation in friction stir welding, *Modelling and Simulation in Materials Science and Engineering* 12 (2004), pp. 143 – 157
  7. M.Z.H. Khandkar, J.A. Khan, A.P. Reynolds: Prediction of temperature distribution and thermal history during friction stir welding: input torque based model, *Science and Technology of Welding and Joining* 8 (2003), pp. 165 – 174
  8. M.Z.H. Khandkar, J.A. Khan, A.P. Reynolds, M. A. Sutton: Predicting residual thermal stresses in friction stir welded metals, *Journal of Materials Processing Technology* 174 (2006), pp. 195 – 203
  9. P. Heurtier, M.J. Jones, C. Desrayaud, J.H. Driver, F. Montheillet, D. Allehaux: Mechanical and thermal modelling of friction stir welding, *Journal of Materials Processing Technology* 171 (2006), pp. 348 – 357
  10. Ø. Frigaard, Ø. Grong, O. T. Midling: A process model for friction stir welding of age hardening aluminum alloys, *Metallurgical and Materials Transactions A* 32A (2001), pp. 1189 – 1200
  11. T.U. Seidel, A.P. Reynolds: Two-dimensional friction stir welding process model based on fluid dynamics, *Science and Technology of Welding and Joining* 8 (2003), pp. 175 – 183
  12. P.A. Colegrove, H.R. Shercliff: CFD modeling of friction stir welding of thick plate 7449 aluminum alloy, *Science and Technology of Welding and Joining* 11 (2006), pp. 429 – 441
  13. A. Arora, R. Nandan, A.P. Reynolds, T. Debroy: Torque, power requirement and stir zone geometry in friction stir welding through modeling and experiments, *Scripta Materialia* 60 (2009), pp. 13 – 16
  14. H. Su, C.S. Wu, A. Pittner, M. Rethmeier: Thermal energy generation and distribution in friction stir welding of aluminum alloys, *Energy* 77 (2014), pp. 720 – 731
  15. H. Su, C.S. Wu, M. Bachmann, M. Rethmeier: Numerical modeling for the effect of pin profiles on thermal and material flow characteristics in friction stir welding, *Materials & Design* 77 (2015), pp. 114 – 125
  16. R. Nandan, G.G. Roy, T.J. Lienert, T. Debroy: Three-dimensional heat and material flow during friction stir welding of mild steel, *Acta Materialia* 55 (2007), pp. 883 – 895
  17. D. Santiago, S. Urquiza, G. Lombera, L. de Vedia: 3D modelling of material flow and temperature in friction stir welding, *Soldagem Insp. Sao Paulo* 14 (2009), pp. 248 – 256
  18. H. Schmidt, J. Hattel: Heat source models in simulation of heat flow in friction stir welding, *International Journal of Offshore and Polar Engineering* 14 (2004), pp. 296 – 304
  19. H. Schmidt, J. Hattel: A local model for the thermomechanical conditions in friction stir welding, *Modelling and Simulation in Materials Science and Engineering* 13 (2005), pp. 77 – 93
  20. N. Dialami, M. Chiumenti, M. Cervera, C. Agelet de Saracibar, J.P. Ponthot: Material flow visualization in friction stir welding via particle tracing, *International Journal of Material Forming* 8 (2015), pp. 167 – 181
  21. N. Dialami, M. Chiumenti, M. Cervera, C. Agelet de Saracibar: An apropos kinematic framework for the numerical modeling of friction stir welding, *Computers and Structures* 117 (2013), pp. 48 – 57
  22. M. Chiumenti, M. Cervera, C. Agelet de Saracibar, N. Dialami: Numerical modeling of friction stir welding processes, *Computer Methods in Applied Mechanics and Engineering* 254 (2013), pp. 353 – 369
  23. P. Bussetta, N. Dialami, R. Boman, M. Chiumenti, C. Agelet de Saracibar, M. Cervera, J.P. Ponthot: Comparison of a fluid and a solid approach for the numerical simulation of friction stir welding with a non-cylindrical pin, *Steel Research International* 85 (2014), pp. 968 – 979
  24. S. Guerdoux, L. Fourment: A 3D numerical simulation of different phases of friction stir welding, *Modelling and Simulation in Materials Science and Engineering* 17 (2009), 075001(32pp)

25. D.M. Neto, P. Neto: Numerical modeling of friction stir welding process: a literature review, *International Journal of Advanced Manufacturing Technology* 65 (2013), pp. 115 – 126
26. J.H. Hattel, M.R. Sonne, C.C. Tutum: Modelling residual stresses in friction stir welding of Al alloys – a review of possibilities and future trends, *International Journal of Advanced Manufacturing Technology* 76 (2015), pp. 1793 – 1805
27. X. He, F. Gu, A. Ball: A review of numerical analysis of friction stir welding, *Progress in Materials Science* 65 (2014), pp. 1 – 66
28. J. Hilgert, H. Schmidt, J.F. dos Santos, N. Huber: Thermal models for bobbin tool friction stir welding, *Journal of Materials Processing Technology* 211 (2011), pp. 197 – 204
29. Z. Zhang, Y.L. Liu, J.T. Chen: Effect of shoulder size on the temperature rise and the material deformation in friction stir welding, *International Journal of Advanced Manufacturing Technology* 45 (2009), pp. 889 – 895
30. M.R. Sonne, C.C. Tutum, J.H. Hattel, A. Simar, B. De Meester: The effect of hardening laws and thermal softening on modeling residual stresses in FSW of aluminum alloy 2024-T3, *Journal of Materials Processing Technology* 213 (2013), pp. 477 – 486
31. N. Dialami, M. Chiumenti, M. Cervera, C. Agelet de Saracibar: Challenges in thermo-mechanical analysis of friction stir welding processes, *Archives of Computational Methods in Engineering* (2016), pp. 1 – 37, doi: 10.1007/s11831-015-9163-y
32. K. Elangovan, V. Balasubramanian, M. Valliappan: Influences of tool pin profile and axial force on the formation of friction stir processing zone in AA6061 aluminium alloy, *International Journal of Advanced Manufacturing Technology* 38 (2008), pp. 285 – 295
33. M. Bachmann, M. Rethmeier, C.S. Wu: Sensitivity analysis of residual stress state in friction stir welding of high strength aluminum alloy, *Materials Testing* 58 (2016), pp. 20 – 26
34. European Deepweld Project. Detailed multi-physics modelling of friction stir welding. Final Report (2008)
35. J.R. Davis. ASM International: *The ASM Specialty Handbook: Aluminium and Aluminium Alloys* (1993)
36. P. Carlone, J.H. Hattel, M.R. Sonne, R. Citarella: Integrated FEM-DBEM simulation of crack propagation in AA2024-T3 FSW butt joints considering manufacturing effects, *Key Engineering Materials* 651 (2015), pp. 877 – 882
37. O.R. Myhr, Ø. Grong: Process modelling applied to 6082-T6 aluminium weldments I. Reaction kinetics, II. Applications of model, *Acta Metallurgica et Materialia* 39 (1991), pp. 2693 – 2708
38. V. Richter-Trummer, E. Suzano, M. Beltrão, A. Roos, J.F. dos Santos, P.M.S.T. de Castro: Influence of the FSW clamping force on the final distortion and residual stress field, *Materials Science and Engineering A* 538 (2012), pp. 81 – 88
39. P. Carlone, G.S. Palazzo: Longitudinal residual stress analysis in AA2024-T3 friction stir welding, *The Open Mechanical Engineering Journal* 7 (2013), pp. 18 – 26